

**FINAL REPORT**  
**RF Exploitation for Tomographic Imaging &**  
**Non-Cooperative Analysis (RETINA)**

---

## Executive Summary

The objective of this project was to develop the RF Exploitation for Tomography Imaging and Non-Cooperative Analysis algorithm (RETINA). The RETINA algorithm is based on Radio Frequency (RF) Tomography, a new sensing paradigm which uses received signal strength (RSS) measurements from mobile and/or stationary devices in an ad-hoc or tactical network to detect (and track objects) in the environment. To further that objective, this project consisted of three primary parts: 1) theoretical algorithm and phenomenological investigation, 2) a field test to acquire live data from a large-scale experiment, and 3) an analysis of the data to confirm the theoretical models and demonstrate a proof of concept.

In the theoretical investigation, a new algorithm was developed to enable joint estimation of stationary objects and moving objects by mobile devices. This algorithm was tested through simulation and shown to be able to either detect and track both moving objects and stationary objects from stationary platforms, or detect stationary objects from mobile platforms. Tracking moving objects from mobile platforms proved more difficult, and the developed algorithm had limited success. Further investigation will be required to improve the robustness of this algorithm when both the objects being tracked and the measurement platforms are mobile.

In the field test, RSS measurements were taken across a large number of paths through a structure. This structure was large, composed of several types of materials and had both an internal column and interior walls. The RSS measurements were generated using this RF tomography testbed, constructed as part of this project. The RSS measurements were formed as a composite from a series of measurements using receivers and transmitters placed at different surveyed positions around the structure.

The measurements from the field test were then analyzed and the RF tomography algorithm developed as part of this project was used to reconstruct the floorplan of the structure. The measurements suffered from some systematic errors which have been identified and can be avoided in future field tests. While the errors reduced the accuracy of the collected data, we were able to produce a reconstruction of the structure's floorplan that is representative of the actual, measured shape of the structure.

This project has met its objective of further development of the RETINA algorithm. A modified version of the RETINA algorithm has been developed that can jointly estimate and track both static and dynamic objects. An RF tomography testbed has been constructed, was field tested, and systematic deficiencies identified and corrected. The data from the field test has been used to reconstruct the shape of an actual structure.

## Contents

Executive Summary.....	ii
Introduction .....	1
Theoretical Analysis and Simulations .....	2
Background .....	2
Tomographic Projection Models.....	2
Line Integral Model .....	3
Elliptical Selection Model.....	3
Fresnel Elliptical Model .....	3
Model Comparison.....	3
Reconstruction Algorithms .....	4
Variance-based Motion Tracking .....	4
Static RETINA.....	5
Dynamic RETINA.....	6
Performance Comparison .....	7
Scenario 1.....	7
Scenario 2.....	8
Test Plan.....	<b>Error! Bookmark not defined.</b>
Overview .....	10
Sounding Configuration .....	10
Sounding Equipment.....	11
Scenarios .....	11
Test Procedure Overview.....	12
The Movement Plan.....	13
The Collection Script .....	<b>Error! Bookmark not defined.</b>
Field Test Data Analysis.....	15
Overview .....	15
Measurement Errors.....	15
Tomographic Reconstruction.....	18
Conclusions and Future Work.....	22
Appendix A: Image Reconstruction Progression (Different Orderings).....	23

## Introduction

In dense networks with large numbers of wireless devices, the received signal strength (RSS) measurements between all the wireless nodes in the network contain a significant amount of information about the environment the network is in. As radio transmissions pass through the environment, the signal is attenuated by the objects it passes through, causing shadowing. If there are sufficient measurements following unique paths in the network, tomography can be used to construct an image of the attenuation in the network. This technique, called Radio Frequency (RF) Tomography is a way to image passive objects using only received signal strength (RSS) measurements. RF tomography has the ability to construct images of the network area, even when there are obstructions or other factors that would limit visibility. For this reason RF tomography can be useful in situations such as locating survivors in rescue operations, determining the structural changes in a structure due to the effects of weapon impacts, and providing comprehensive intelligence for tactical assaults. In this project, we worked to improve the technological readiness of this promising technique.

## Theoretical Analysis and Simulations

In this section, we describe the theoretical background of RF tomography, introduce several new and existing shadowing models, describe several existing and new reconstruction algorithms, and evaluate the reconstruction algorithms through simulation.

### Background

Tomography is the method of imaging a planar section of an object, through the use of a penetrating wave, such as the use of x-rays in medical imaging computed axial tomography (CAT) scans, sometimes referred to as computed tomography (CT) scans. In CT scans, a circular array of x-ray emitters and receivers are positioned around the object of interest. The total path loss between the transmitters and receivers can be used to determine the spatial loss field (SLF). This spatial loss field represents how much each point in space contributes to the total path loss experienced across all of the measured paths, and is effectively a cross-sectional image of the object. For practical purposes, the spatial loss field is always discretized so that instead of representing how every point in space contributes to the total path loss, it aggregates the points into pixels (or voxels) and describes how much each pixel contributes to the total path loss. For example, consider Figure 1. In Figure 1.a we have several transceivers (red circles) which take path loss measurements across each of the (black) paths to the other transceivers. Using a tomographic projection model, which is a function that determines how the spatial loss field affects each of the path loss measurements, these path loss measurements can be transformed into the reconstructed image found in Figure 1.b.

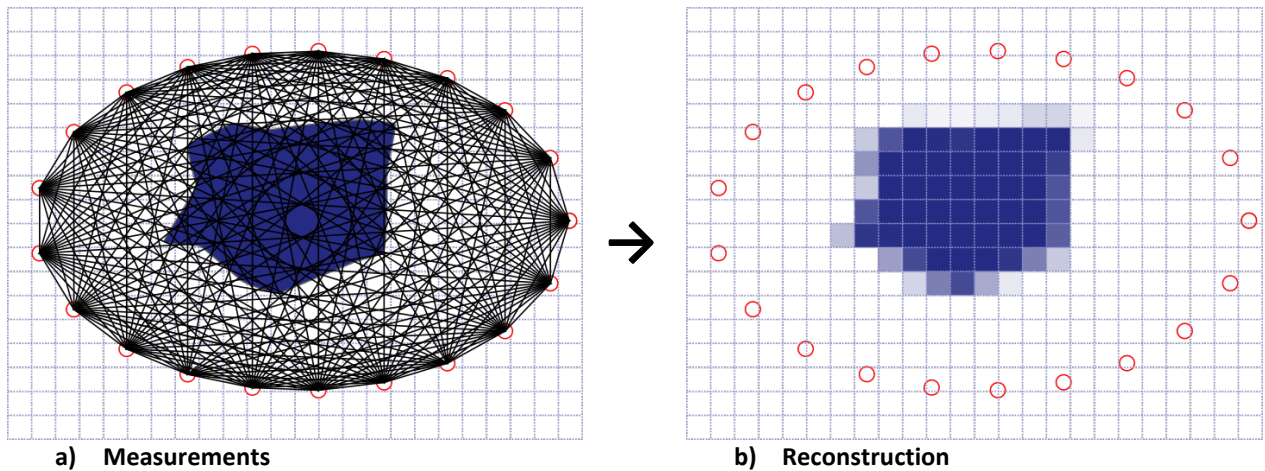


Figure 1: Tomography Example

### Tomographic Projection Models

Tomographic imaging is not constrained to paths made by x-rays or to applications in medical imaging. It can be also used with radio frequency signals, however, the lower frequency of the radio signals and the relatively longer ranges mean that electromagnetic effects such as diffraction and reflection may need to be considered. For simplicity, we will only consider linear tomographic projection models. This means that the tomographic projection  $\mathbf{b}$  can be represented as a vector

whose dot product with the discretized spatial loss field  $\mathbf{g}$  is proportional to the path loss (in dB) and the entire collection of path loss measurements represented by the matrix product  $\mathbf{B}\mathbf{g}$ . To recover the spatial loss field from the measurements we apply the inverse transform  $\mathbf{B}^{-1}$  to project the measurements back into the spatial loss field. In most cases, however this inversion is not possible since  $\mathbf{B}$  is singular. To compensate for this, regularization techniques such as Tikhonov regularization are applied. We describe two existing and one new tomographic projection model below and discuss their merits.

### Line Integral Model

In this model, the path loss from shadowing is assumed to be proportional to a line integral across the spatial loss field. For the discretized spatial loss field, the tomographic projection consists of a vector of weights with entries equal to length of the path that falls within the corresponding pixel. This is the most common model used in CT, and a modification for RF Tomography was introduced as the Network Shadowing Model (NeSH). The NeSH model differs from traditional tomographic line integral model in that the proportionality constant is a function of the path length. This modification was made so that the model matches the larger scale shadowing statistical models. It was necessary because this model does not consider the effects of diffraction at all. This modification only changes the large scale statistics. This means that, even with this modification, diffraction will cause significant artifacts in the reconstruction.

### Elliptical Selection Model

In this model, the tomographic projection consists of a selection vector with entries of either 0 or 1 depending on whether the center of the pixel is within the ellipse that has the positions of the transmitter and receiver as foci. This model has also been previously used for RF Tomography. There is some physical justification for using an ellipse, as the well-known Fresnel zone has an ellipsoidal shape. A problem with this model is that there is not a good physical basis for determining the parameters of the ellipse. Current methods using this model find the parameters of the ellipse through trial and error. Additionally the decision to set the weights of all of the pixels equally has no physical justification.

### Fresnel Elliptical Model

We created a model based on the Fresnel zone ellipsoid. In this model, the weights are equal to the inverse of the area of the smallest ellipse having the transmitter and receiver as foci which contains the center of a given pixel. This model is more complicated than the elliptical selection model, but should better capture the relative strengths of diffracted paths.

### Model Comparison

The weights chosen by the three tomographic projection models are compared visually in Figure 2.

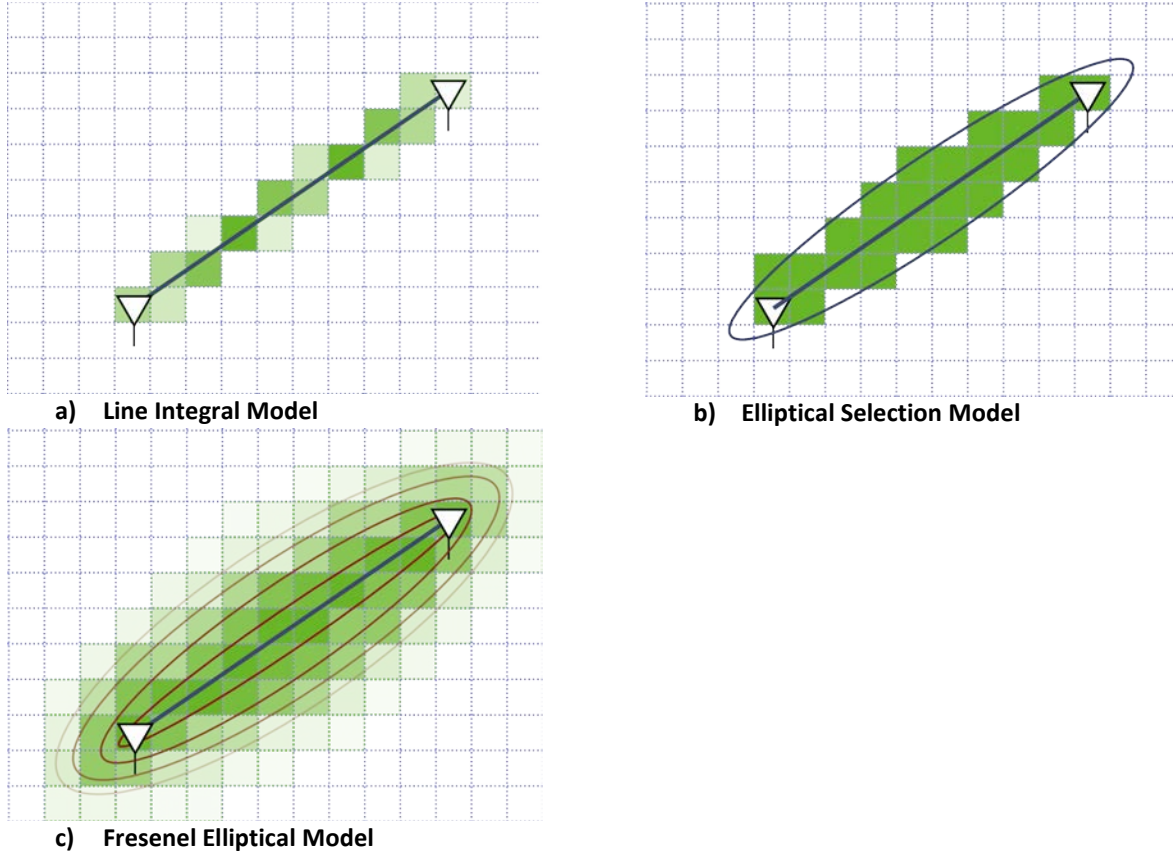


Figure 2: Example weight vectors for the three tomographic models

## Reconstruction Algorithms

In this section we examine several existing reconstruction algorithms and identify their limitations.

### Variance-based Motion Tracking

We first consider the variance-based motion tracking introduced by Wilson et. al [Wilson et. al 2011]. This algorithm only considers applications where the transmitters and receivers are stationary. In this algorithm, the windowed sample mean and variance of the RSS measurements is calculated, and then the variance is back-projected into the spatial loss field using the tomographic projection model. A diagram of this technique is shown in Figure 3. This technique, as originally proposed, does not detect

static objects; however an estimate can be obtained by back-projecting the sample mean.

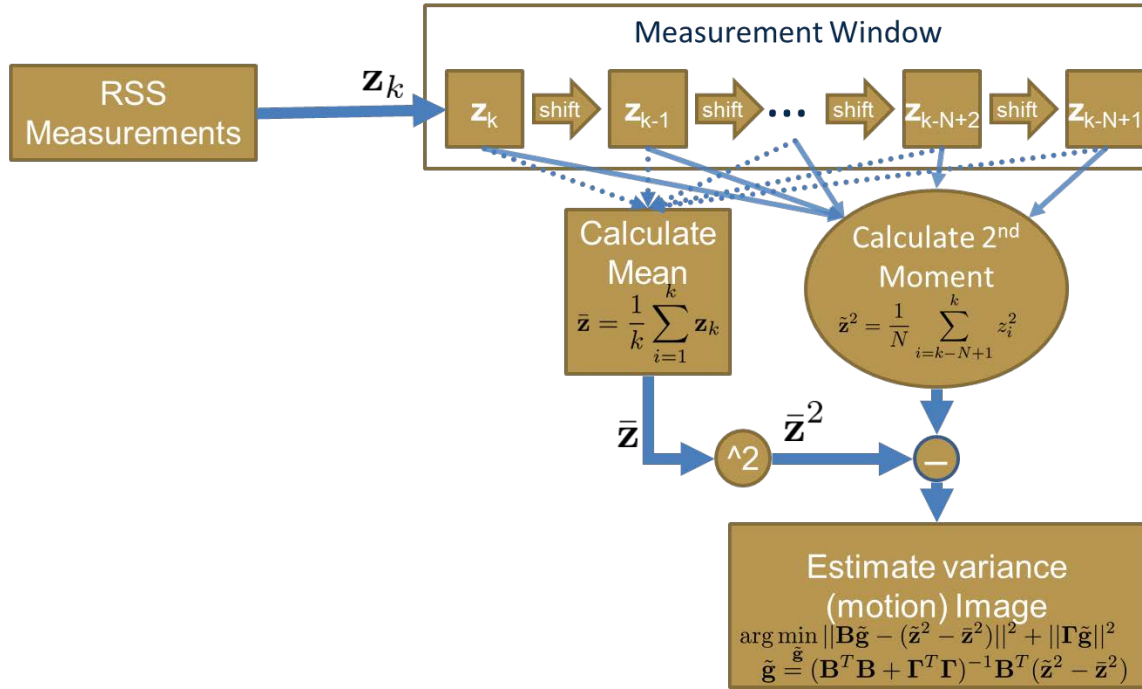


**Figure 3: The variance-based motion tracking algorithm**

This technique has a number of limitations. The primary limitation is that it does not show where moving objects are, but instead shows a streak from where they were, to where they are. The length of this streak is determined by the speed of the object and the size of the measurement window. Reducing the size of the measurement window will place the streak closer to the object's present location, but will also increase the noise in the reconstruction. Another major limitation of this technique is that it cannot be easily modified to work with measurements from mobile devices.

### Static RETINA

The original static RETINA algorithm developed at GTRI avoids most of these issues. In this algorithm, the RSS measurements are taken directly and an extended Kalman filter is used to estimate the spatial loss field. The flexibility of reconstructing directly from the RSS measurements allows this algorithm to work with measurements from mobile devices. However, this technique was not designed to detect and track motion, and there appears to be no simple modification to make it track motion well. Further, while the extended Kalman filter helps deal with the non-Gaussian measurement noise, it is complicated and highly dependent on the tomographic projection model. A diagram of this technique is shown in Figure 4.



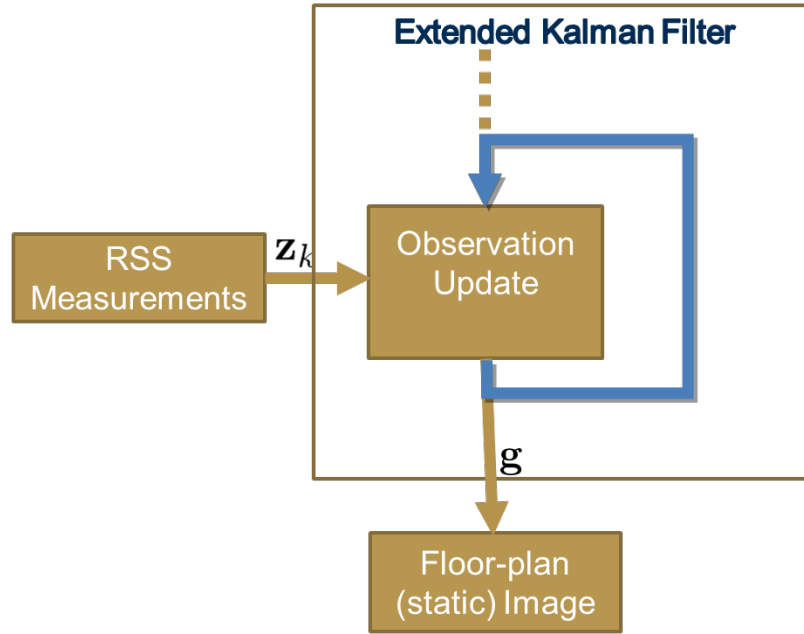


**Figure 4: The Static RETINA algorithm**

### Dynamic RETINA

The Dynamic RETINA algorithm developed during the course of this project improves on both existing methods. It jointly estimates both the floor plan image and the motion image. It incorporates a motion model, where the mobile entities that it is tracking are assumed to move according to an auto-regressive (AR) position model where the probability density of their position in the next frame is a Gaussian centered on their position in the current frame. This particular model is efficient because it can be implemented as a 2D Gaussian blur on the motion image with a corresponding adjustment to the covariance estimate. Since it incorporates a motion model, it is able to more accurately detect and track moving objects, avoiding the problems in the variance-based technique. It also avoids the complexity and model dependence of the extended Kalman filter in Static RETINA by using a Kalman Filter instead, and approximating the measurement noise as Gaussian. The algorithm should be able to detect and track moving and static objects from mobile or stationary platforms. A diagram of this algorithm is shown in Figure 5.

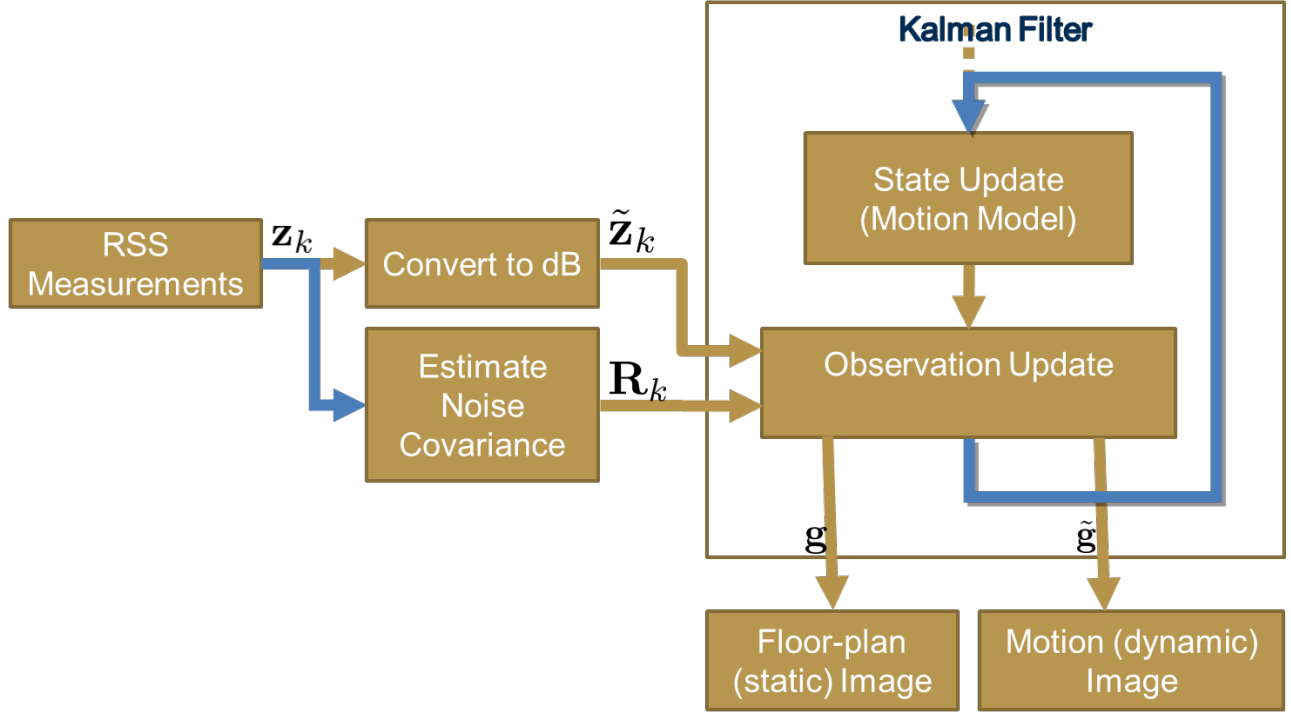


Figure 5: Dynamic RETINA algorithm

## Performance Comparison

In this section we will compare the performance of the above reconstruction algorithms through simulation.

### Scenario 1

We will first consider a network of 28 stationary nodes, placed around the perimeter of the area of interest. The area of interest contains a building with 5 moving entities. The moving entities' actual positions are marked with black circles. The static and dynamic reconstruction estimates from the 3000<sup>th</sup> frame are shown in Figure 6. Note that the estimates of the static reconstruction are almost identical for both techniques. This is expected since the tomographic projection is linear and in the absence of mobile nodes, taking the average RSS and then back-projecting is equivalent to taking the average of the back-projected RSS. The estimates of the dynamic reconstruction are very different. The variance-based reconstruction only shows areas where the SLF has changed over the measurement window, leaving streaks of high variance. In contrast, Dynamic RETINA tracks the moving objects based on its motion model, allowing it to very accurately track the position of the mobile entities as they move around the network area.

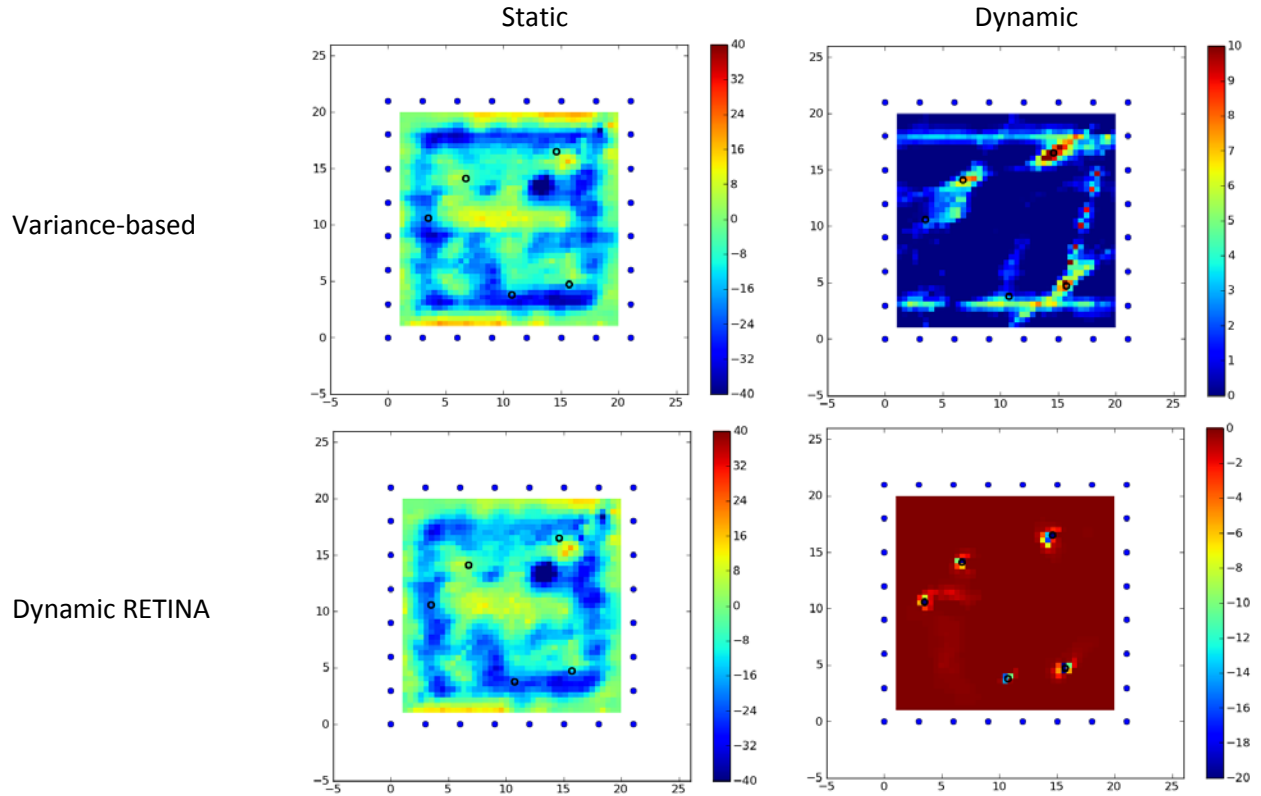
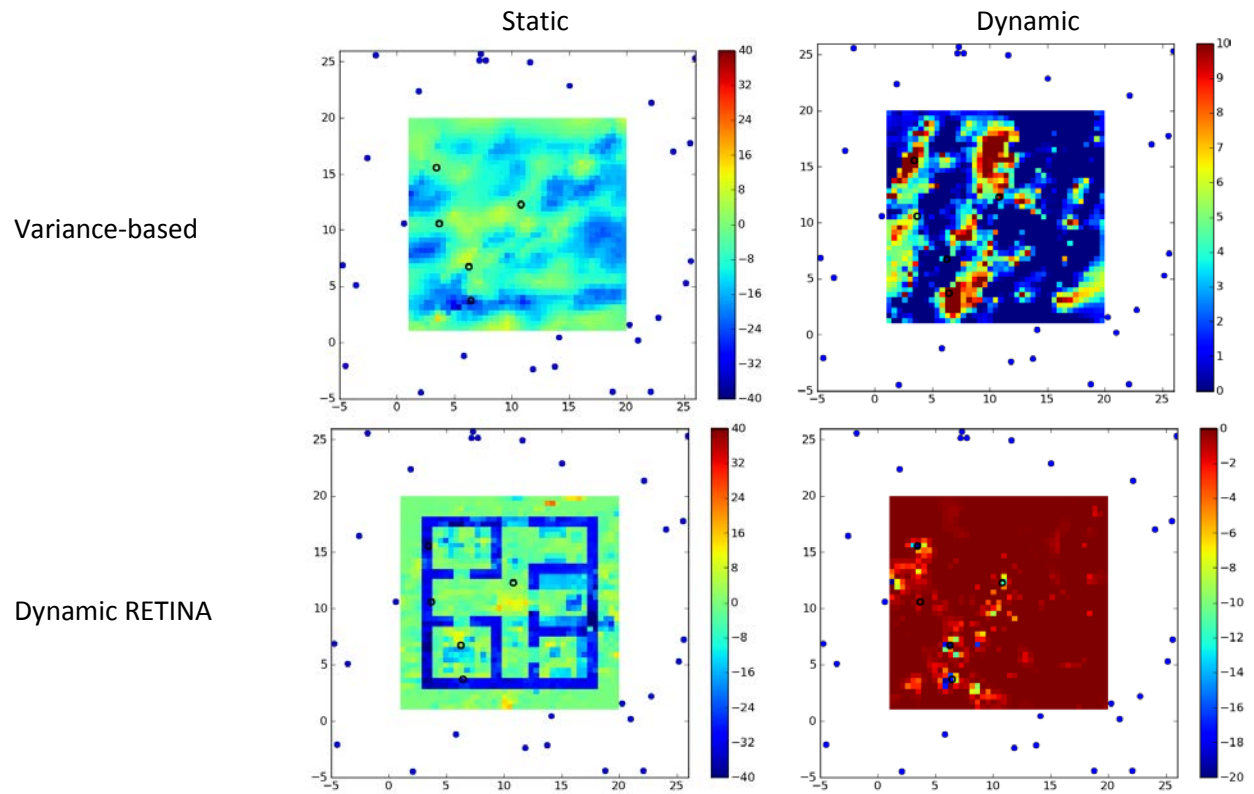


Figure 6: Comparison of the Variance-based reconstruction with Dynamic RETINA (Static Network)

## Scenario 2

We will first consider a network of 28 nodes moving according to a random direction model. These nodes are constrained to travel outside the area of interest. The area of interest contains a building with 5 moving entities. The moving entities' actual positions are marked with black circles. The static and dynamic reconstruction estimates from the 400<sup>th</sup> frame are shown in Figure 7. Since the nodes that were taking the measurements were moving in this example, the Variance-based reconstruction performed poorly. Its static reconstruction is severely blurred and distorted, while the motion tracking reconstruction doesn't appear to work at all. In contrast, the static reconstruction from Dynamic RETINA is even clearer than the static node case. Dynamic RETINA does appear to have some problems tracking mobile entities from mobile nodes. In the figure, it only has correctly tracked 4 of the 5 entities.



**Figure 7: Comparison of the Variance-based reconstruction with Dynamic RETINA (Dynamic Network)**

## Field Test

### Overview

To determine how well the RETINA algorithm will work with true RF data, GTRI performed a field collection of RF samples using various stationary RF transmitters and receivers. Each collection point represented a possible position of a mobile node at a given time. By collecting a large number of path loss values for various path pairs, we have the ability to exercise the GTRI RETINA algorithm over a large number of arbitrary movement paths. Furthermore, by sounding from predefined stationary points, we can remove a large amount of position uncertainty from the algorithm to determine the RETINA performance when all nodes are localized. To drive down the position uncertainty, we employed surveying techniques along with laser rangefinders to precisely place nodes.

We field tested two scenarios. The first scenario was a control test, where the channel sounding was performed without any objects in the imaging space. In the second scenario, we imaged a makeshift structure composed of plywood, sheetrock, concrete board and cinderblock. The channel sounding equipment consisted of 10 Agilent E443x signal generators as the transmitters and 10 Ettus USRP2 software defined radios as the receivers. This 10 X 10 setup allowed us to sound 100 links per position. We will perform the sounding over a 21X21 grid per scenario.

### Sounding Configuration

The sounding points were measured using tape measure relative to the four designated corners of the sounding grid. This allowed us to setup a relative coordinate system for the measurement campaign. Figure 1 shows the sounding grid configuration.

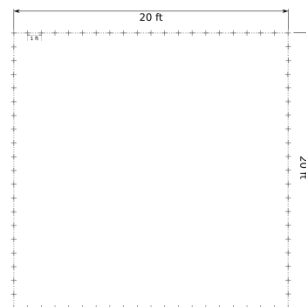


**Figure 8: Sounding grid configuration.**

Each Rx antenna (10) and each Tx antenna (10) was be affixed to a tripod, which was moved to the pre-surveyed points during each reposition. Sounding waveforms were be preloaded on to each Agilent E443x which continuously transmitted throughout the test at the sounding frequency of 2.425GHz with 5MHz bandwidth. Each E443x was synchronized to an atomic clock source to ensure frequency stability.

Each Rx antenna was connected to an USRP2 which was in turn connected to a host laptop running Linux. The USRP2s were also be synchronized to an atomic clock to ensure frequency stability.

The USRP2 host laptops were all be networked to a central computer in the field, where they were remotely controlled. For each sounding position, the USRP2s were remotely instructed to record for a period of several milliseconds. This IQ data was stored on the host laptop and then uploaded to the central computer for processing and analysis.

## Sounding Equipment

- 10 Agilent E443x Signal Generators
- 10 USRP2s
- 10 2.4GHz USRP2 Rx cards
- 10 host laptops
- 20 2.4GHz antennas
- 2 Rubidium Atomic clocks
- 20 clock cables
- 20 RF cables
- 20 Tripods
- 1 laser rangefinder
- 1 master control computer

## Scenarios

The first sounding scenario was used to collect control data and will be performed without any objects in the link paths. This control data allowed us to calibrate the channel measurements in a benign environment. The second sounding scenario was performed with a building in the image area. Figure 2 gives a schematic of the two scenarios.

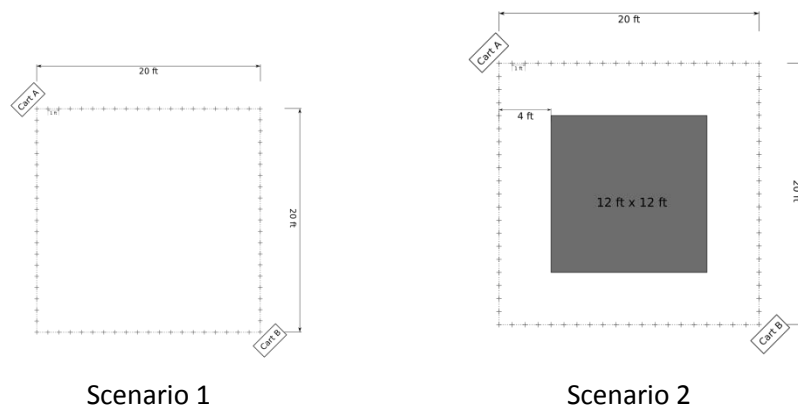


**Figure 9: Scenario 1 and 2.**

The building was be constructed primarily of three building materials: wood, sheetrock, concrete board, and cinderblock. A rough floor plan of the building is given in Figure 3. Each wall was composed of 3

modular 8' high by 4' wide panels supported by a 2X4 wood stud assembly. We constructed a total of 13 panels with the following breakdown:

- 3 3/8" plywood panels
- 3 1/2" OSB panels
- 1 interior wall sheetrock panel
- 3 Exterior wall sheetrock/plywood panels
- 3 concrete board panels
- 1 column of cinder blocks

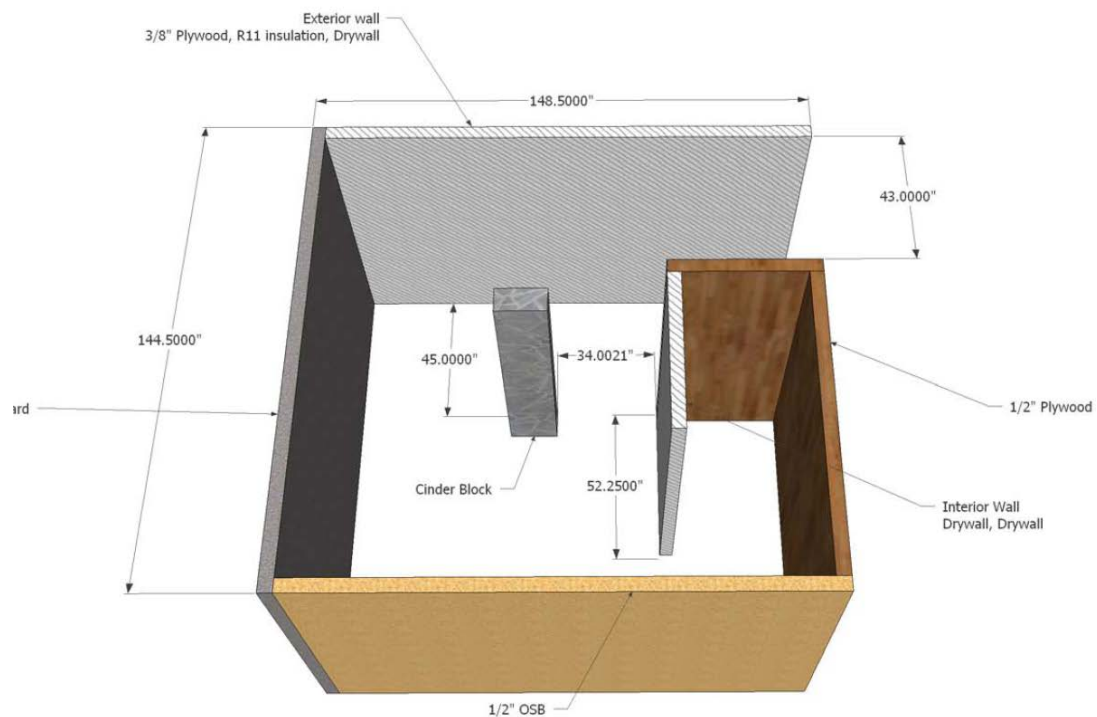


**Figure 10: Building configuration.**

## Test Procedure Overview

The test procedure consisted of three stages: setup, survey, and test. The setup and survey phases were executed concurrently.

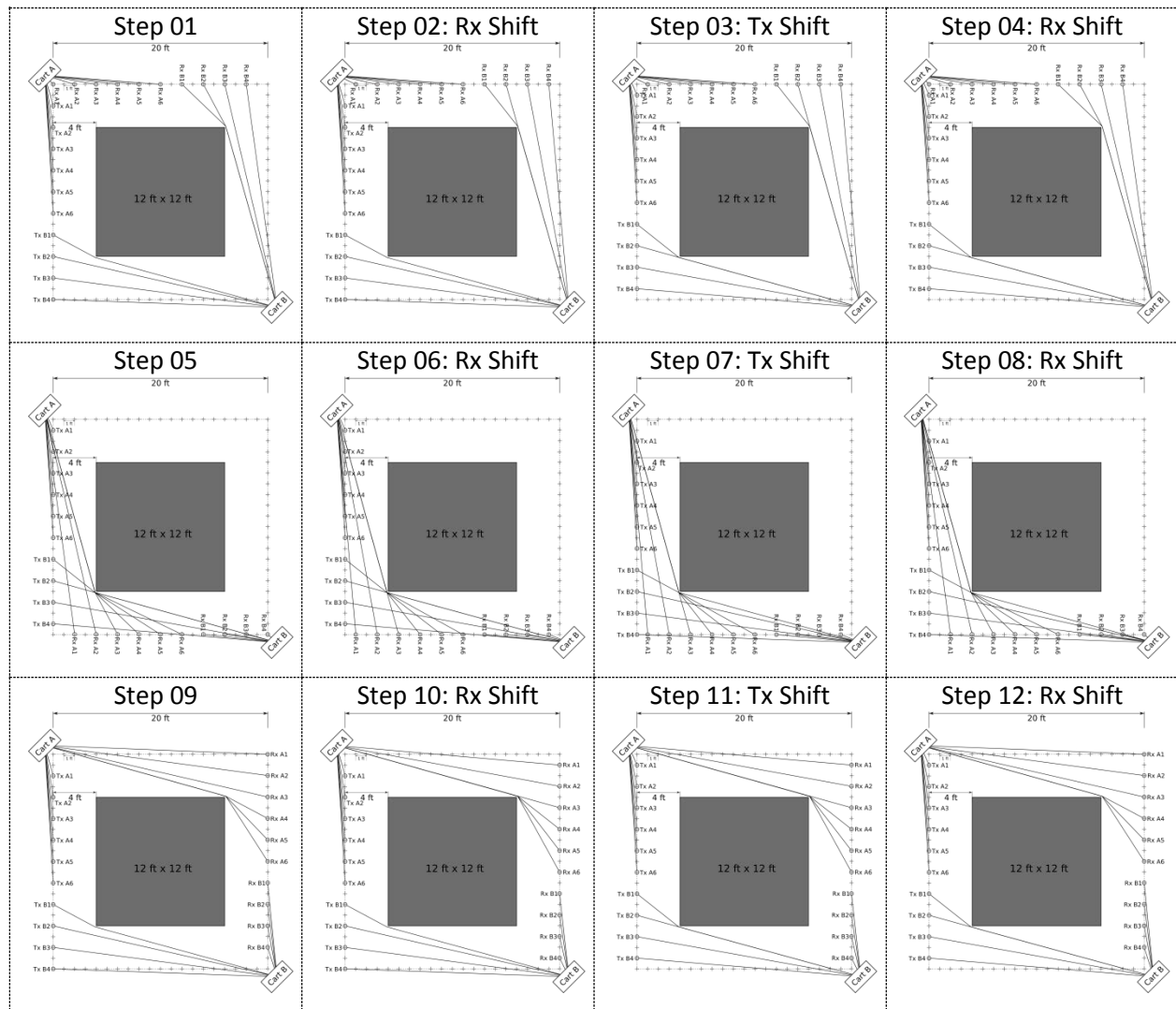
During the setup phase, the equipment was unloaded, tested, and prepared for data collection. Additionally, the structure to be imaged was constructed. The equipment divided into two carts: Cart A, which hosted 6 transmitters and 6 receivers, and Cart B, which hosted 4 transmitters and 4 receivers. Each cart was connected to an independent EU3000 Honda generator to provide power. The central computer was co-located with Cart B and connected to the control network.

During the survey phase, we constructed the 20' square perimeter collection grid and placed a marker approximately every 1' around the perimeter.

During the testing phase, all of the signal generators were set to continuously transmit the orthogonal sounding waveforms. Sounding the links between all the marked positions required measurements from multiple positions. At each position the central computer initiated data collection and verified that all 100 measurements were reasonable. Between measurements the antennas were moved according to the following movement plan.

## The Movement Plan

The set of movements consisted of 18 simple movements or 'shifts,' where either the transmitting antennas or receiving antennas were moved 1' to the adjacent marked position, and 5 complex movements where a set of antennas were moved from one side of the sounding region to another. A complete sounding required 24 steps, described visually in Figure 4.





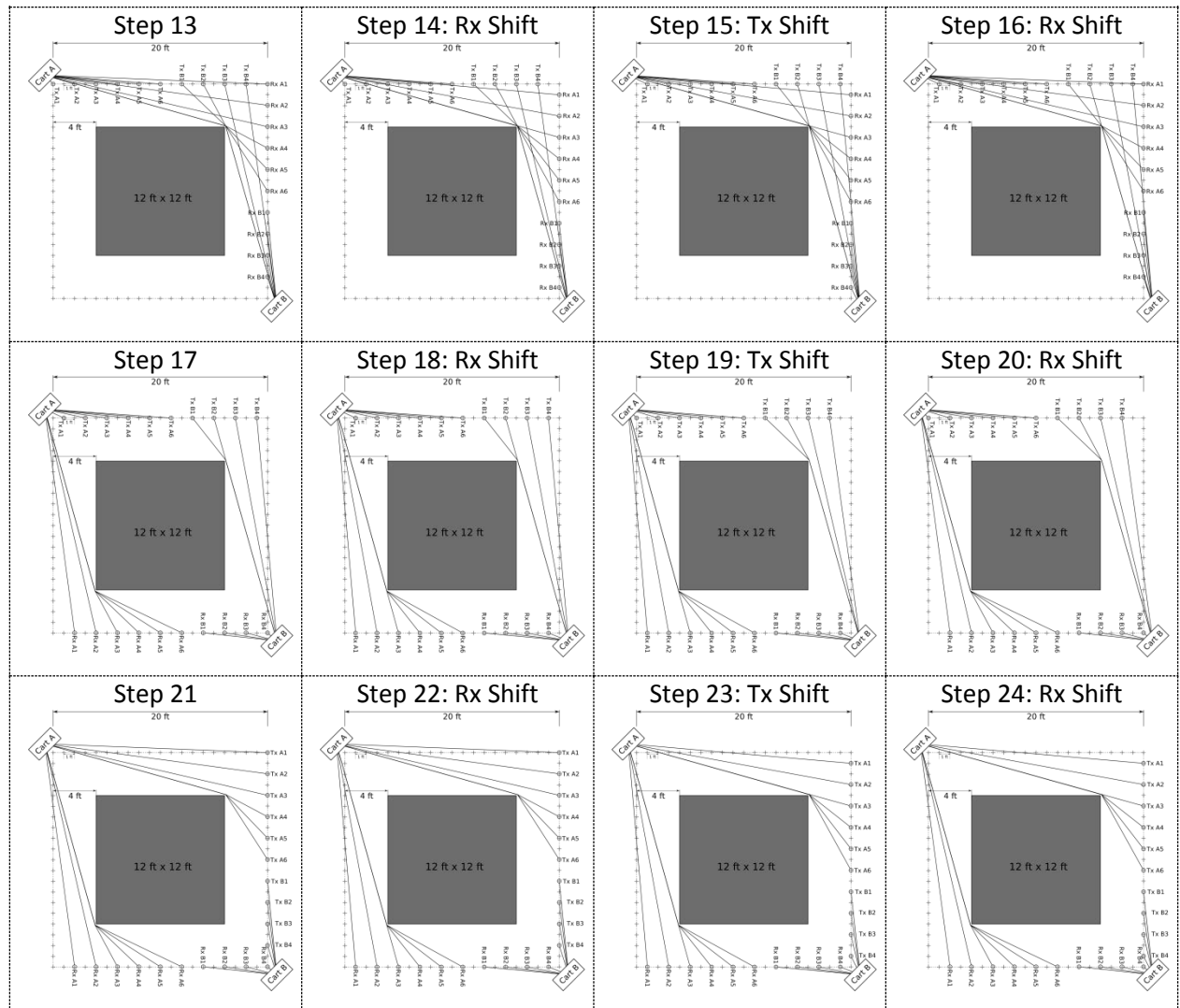


Figure 11: Data Collection Sequence

## Field Test Data Analysis

### Overview

The field test data was collected as described in the Test Plan, and analyzed as described below. Despite the planning and preparation that went into the field test, the collected received signal strength (RSS) data suffered from unexpected sources of interference and distortion, which complicated analysis and tomographic reconstruction of the structure. Further, the estimates of the relative position of the nodes and the structure proved to be less accurate than expected. In this analysis we identify the sources of these errors, discuss how we compensated for them, and propose methods to alter the experimental setup to eliminate or mitigate these sources of error. We then present our successful tomographic reconstruction of the structure from the (RSS) measurements.

### Measurement Errors

In our analysis we found systematic errors in both the RSS and distance measurements. The RSS signal strength measurements were perturbed by two unexpected effects: interference between transmitters and distortion in the receiver, while the distance measurements were less accurate than anticipated.

#### *Interference*

In the field test, each transmitter was transmitting a different orthogonal sequence. This means that even though they were transmitting at the same frequencies at the same time, the receivers can isolate the signal from each transmitter by convolving the received signal with the sequence for that transmitter. Since the transmitted sequences are orthogonal, we did not expect any interference between them. This assumption was supported by our preliminary laboratory experimentation where there was no observable interference between transmitters at the receiver.

In the raw data recorded during the field test, however, this interference was observed to be significant. Further analysis revealed that the cause of this interference was synchronization error. In the field test, the transmitters and receivers were split between two carts. All of the receivers and transmitters on a cart were synchronized to an atomic clock, also on the cart. However, the atomic clocks on the two carts were not synchronized with each other. While the atomic clocks still provided stability, there was a small, static frequency offset between the two carts. This had two primary effects on the recorded signal: carrier frequency offset and sampling frequency offset. We were able to estimate both of these offsets and apply successive interference cancellation to remove most of the interference. In future tests, we can avoid this problem by either abandoning the orthogonal transmission waveforms or ensuring that the atomic clocks are synchronized.

#### *Distortion*

The measurements from the field test also showed severe distortion. In free space the power in a wireless signal is supposed to decrease with the square of the distance, so the RSS should have decreased linearly with distance. Plotting the RSS measurements against measured distance, showed no clear relationship between distance and RSS, even for the measurements when the structure was absent. A plot showing these results for receiver 1 is shown in Figure 1. While some of the

measurements do appear to have the appropriate slope, the majority are clustered in the outlying group with long distances and high RSS measurements.

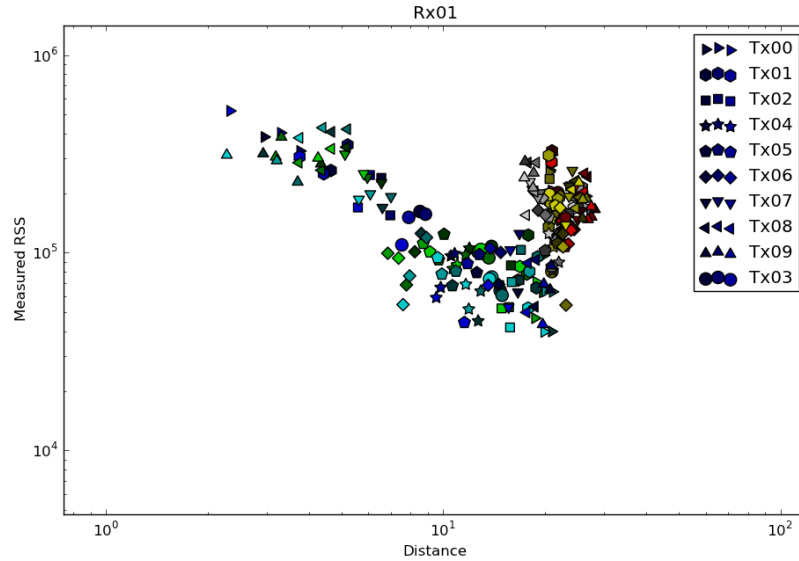


**Figure 1: Measured RSS vs. Distance in the absence of the structure**

Through a series of laboratory tests to replicate the problem and a detailed analysis of the design of the receiver front-end, this problem was eventually traced to a configuration problem in the receivers. The receiver gain was set too high, so the amplifiers in the receiver were in saturation. We characterized the response of the receiver power amplifier by sending a series of ramp signals and measuring the receiver response. The normalized results are shown in Figure 5. Since we are plotting the normalized output vs. input from the ramp signal, and the ramp has portions of both increasing and decreasing power, the power response traces two slightly different paths. The red rectangle shows the region that the receivers were determined to be operating in during the field test. This region is very far from being linear, and is not even monotonic. Since the receivers were operating in this region, the received signal measurements will appear to be independent of received power.

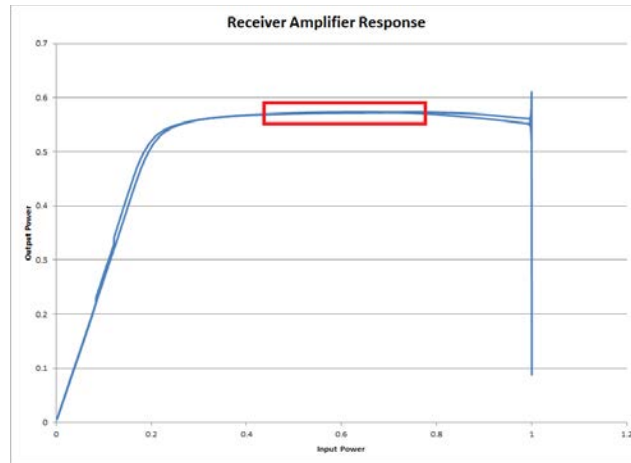


**Figure 12: Receiver amplifier response curve.**

Such distortion would normally make the measurements unusable for RF tomography because the received signal would have no information about the amount of attenuation encountered on the transmission path. In this case, however, the transmitters were transmitting simultaneously, with long, orthogonal sequences. Although the received signal contains no information about the received power, the relative power among the different transmitters was preserved and is reflected in the RSS measurements. The problem then becomes a calibration problem where we determine the power offset of each receiver at each step in the measurements. Further, in most of the steps, there was a line-of-sight path from each receiver to at least one transmitter. The largest such RSS measurement was compared against the expected free-space RSS to determine the receiver power offset. In the absence of a line-of-sight path, the path with the largest RSS measurement was used. This correction mitigates the most significant effects of the distortion, but cannot completely correct for it. In future tests, this problem can be avoided by configuring the receiver gain based on additional calibration measurements.

### *Distance Measurements*

During the field test, we conducted numerous distance measurements to determine the relative position of the transmitters, receivers and the structure. During the site survey portion of the field test we marked off the perimeter of a 20' square at 1' intervals for placement of the receiving and transmitting antennas. To form this square, we measured both the lengths of the edges and diagonals. We then marked off 3 of the edges and waited for the structure to be complete before measuring and marking the final edge. Unfortunately, the resulting shape was not square. The final edge was over 1 foot too long. We attribute this error due to the curvature of the ground in at the test site. If the ground were flat, measuring the edges and diagonals would be sufficient to ensure the grid was square. However, since the ground was not flat, the measuring tape used for these measurements was deflected by the ground and these measurements were not taken in perfectly straight lines. To compensate for the unexpected positions of the antennas, additional measurements were taken from several of the marked off positions and points on the structure. Additionally, the size and shape of the structure were precisely measured. During analysis, geometrical constraints on the shape and position of both the structure and the nodes made it apparent that these measurements could not be as precise as expected. This made the problem of reconstructing actual positions that the antennas were located

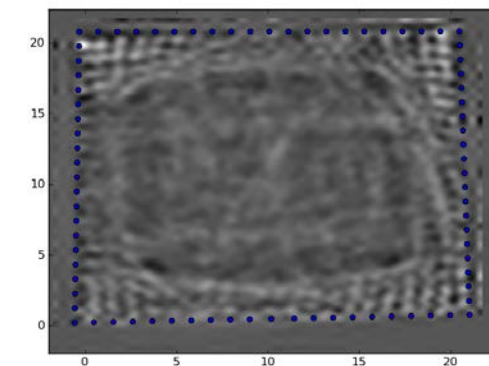
quite difficult. In the end we used a nonlinear optimization to estimate the position of both the nodes and the structure, and the resulting position estimates are less than a foot from of the actual positions.

There are several potential causes for the distance measurement error and the resulting inconsistency. Measurements were made at antenna height, were only approximately level, and were not necessarily repeatable. In future tests, we should allocate more time and resources to conduct the tests or develop a jig to guarantee repeatable precision measurements.

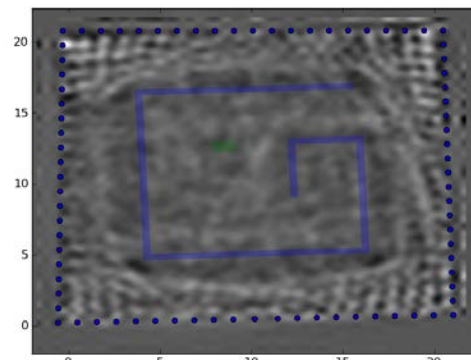
## Tomographic Reconstruction

Despite the problems identified with the data collected, we were able to get a reasonable tomographic reconstruction of the structure. One objective of this project was to understand how well various tomographic projection models compare to actual measurements. To this end, we performed a tomographic reconstruction using each of the models described in “Tomographic Projection Models.”

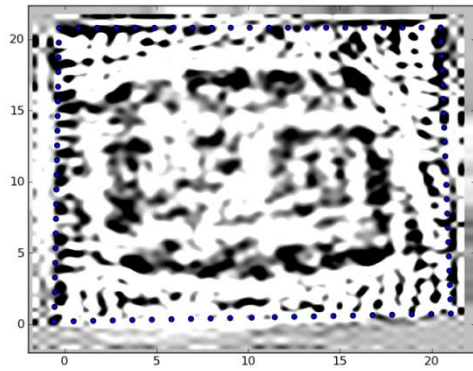
We show the reconstruction using the Fresnel Elliptical model in Figure 13, and the reconstruction using the Elliptical Selection algorithm in Figure 14. In these figures we show both the raw reconstruction as well as a contrast-enhanced version. For comparison, we also show an overlay of the shape of the structure. Both reconstructions recover the shape of the structure. From the figures, the Fresnel Elliptical model was able to keep more of the hard lines from the structure and has less blurring near the internal wall, but has more artifacts near the edges of the image. The Elliptical Selection model in contrast, blurred the lines from the structure more, but has fewer artifacts. From the available data, we are unable to determine which model best matches the data set. Further data collection and analysis will be necessary to determine which model most accurately reflects the physical reality. Due to their similarity, the remainder of this analysis will only discuss the results from the Elliptical Selection model, shown in Figure 14.



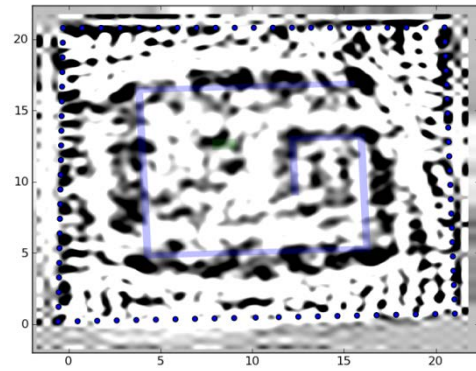
a) Raw Reconstruction



b) Raw Reconstruction (with structure overlay)

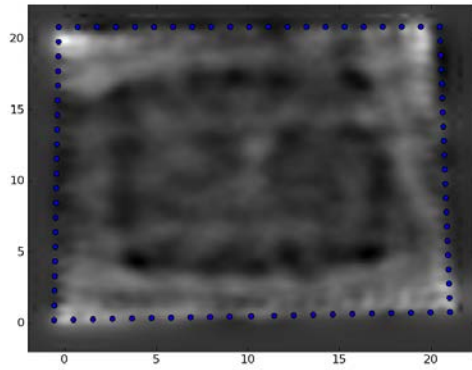


c) Reconstruction (contrast enhanced)

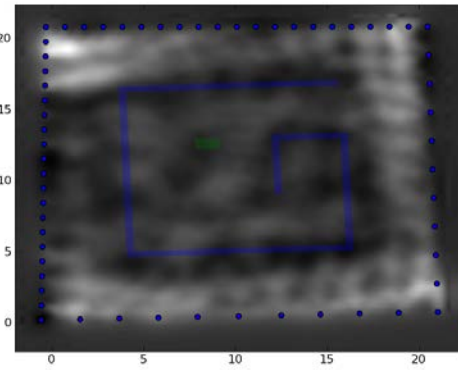


d) Reconstruction (overlay, contrast enhanced)

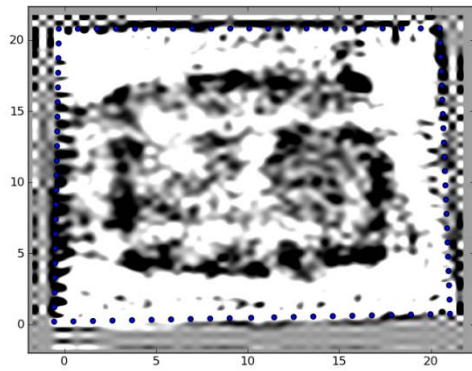
Figure 13: RSS based reconstruction of structure (Fresnel Elliptical Model)



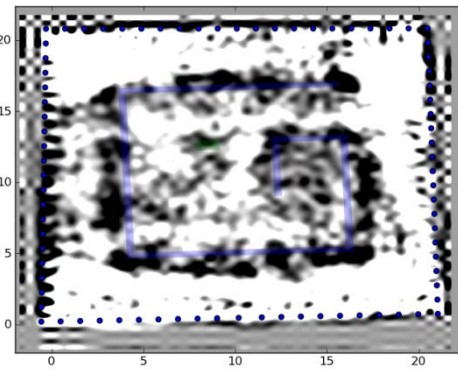
a) Raw Reconstruction



b) Raw Reconstruction (with structure overlay)



c) Reconstruction (contrast enhanced)



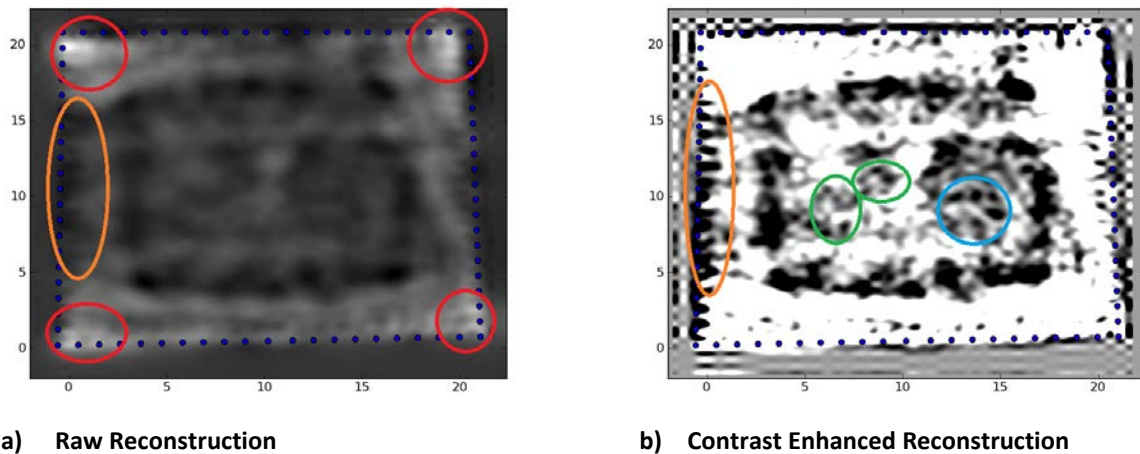
d) Reconstruction (overlay, contrast enhanced)

Figure 14: RSS based reconstruction of structure (Elliptical Selection Model)

In addition to the structure clearly standing out from the background, some additional details can be seen in the contrast-enhanced image shown in Figure 14.c. The structure was constructed of 4' wide panels (8' tall), which were joined at the edges to construct the 12' walls. At the point where the panels join, the boards framing one the panel are attached to the boards framing the other panel. This

effectively creates ‘pillars’ composed of 2 sets of framing studs where the panels join. Since the panels are 4’ wide, we would expect to see one of these ‘pillars’ on each corner and two equally spaced in between. Such ‘pillars’ can be clearly seen on the left side of Figure 14.c, and are somewhat less clearly visible on the other walls.

While the reconstruction shows the structure quite well, there are some artifacts in the reconstructed image. We highlight these artifacts in Figure 15. Two types of artifacts appear outside of the structure. Theoretically the spatial loss field outside the structure should be 0, since there is nothing to cause shadowing. Instead, the reconstruction has a large negative attenuation (gain) near the corners. This appears as the white regions shown within red circles in Figure 15.a. Further, the left side has a relatively large attenuation. This appears as the darker area of the image, circled in orange in Figure 6.a and Figure 15.b. There are also artifacts in the reconstruction of the structure itself. The cinder block appears to have artifacts below and to the left of it (circled in green in Figure 15.b). The inner wall has some artifacts between it and the outer wall (circled in blue in Figure 15.b). There are many possible causes of these deviations. Such causes include the position error, the distortion in the RSS measurements, and imperfections in the shadowing model. Additionally, the artifacts inside the structure could also occur if the measurements for some of the receivers or transmitters were swapped for a few of the measurement steps. Such a swap would cause an artifact that would look like a distorted, rotated floorplan superimposed on the reconstruction, which would cause artifacts from the inner wall and cinder block to appear. Further work will be needed to isolate the cause of these artifacts.

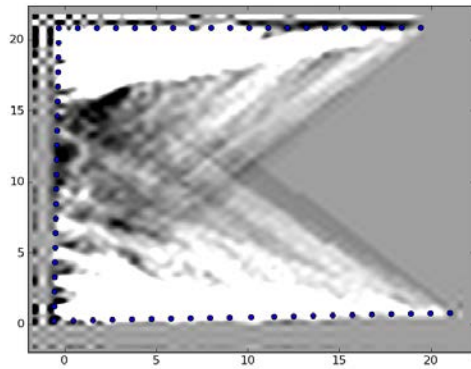


**Figure 15: Artifacts in Reconstructed Images**

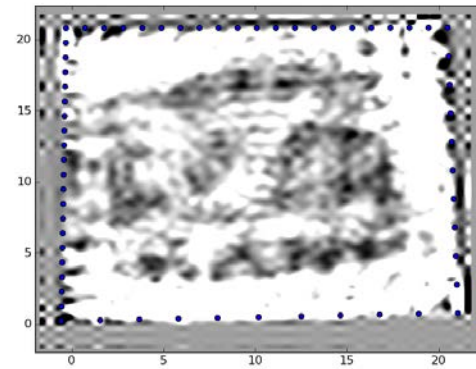
In addition to the tomographic reconstruction using the full dataset, we performed a limited investigation into the amount of data required to form a useable reconstruction. For example, we consider the reconstruction using only the data from 5 of the 24 collection steps. Two examples of this are shown in Figure 16. In Figure 16.a, we try to reconstruct the floorplan with the first 5 measurement steps. From the data collection sequence (previously shown in Figure 11), the first 5 measurement steps mostly just cover the upper left corner of the building. For this reason, these measurements are not



independent enough to image the building. In Figure 16.b, we instead use the measurements from steps 1, 5, 9, 13, 17, and 21. Since these are the most independent measurements, we are still able to achieve a reasonable reconstruction. Further analysis is needed, however, to objectively how the number and type of samples will affect reconstruction accuracy and how this is affected by the structural characteristics of the object being imaged. A detailed chart comparing the reconstruction using different sets of measurements is shown in Appendix A.



a) Reconstruction with Steps 1-5



b) Reconstruction with Steps 1,5,9,13,17,21

Figure 16: Reconstructions from only 5 data collection steps

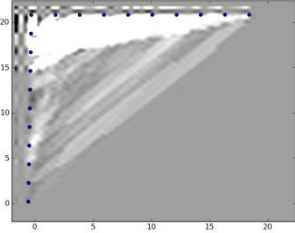
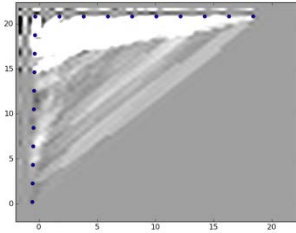
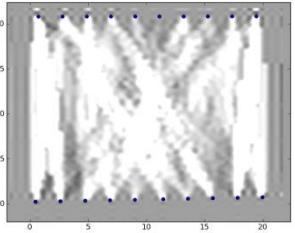
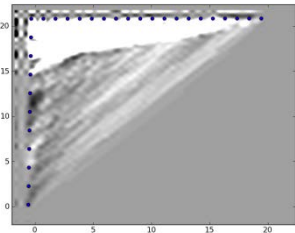
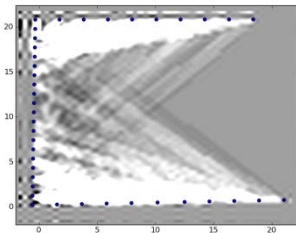
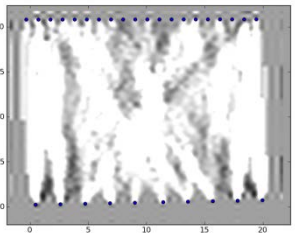
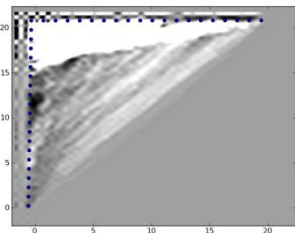
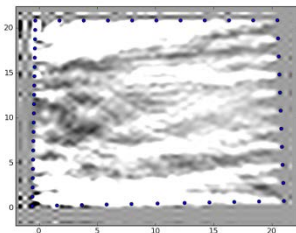
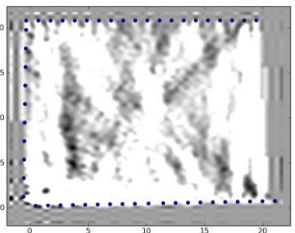
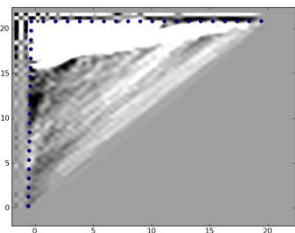
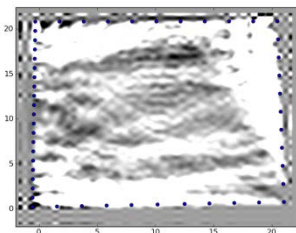
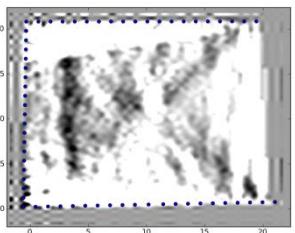
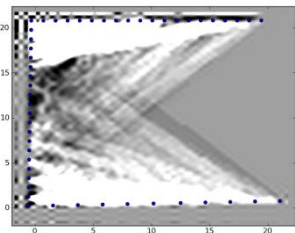
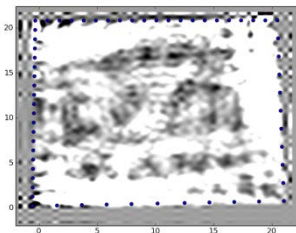
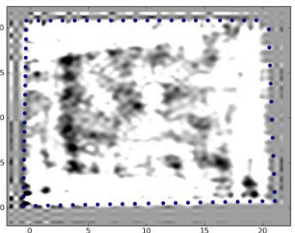


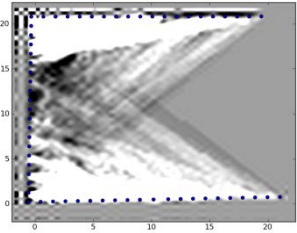
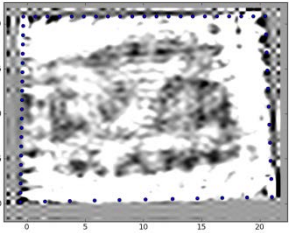
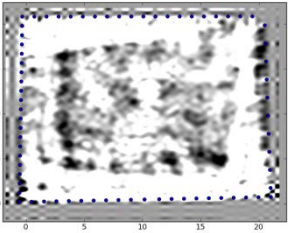
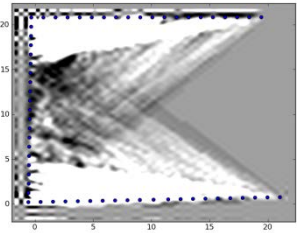
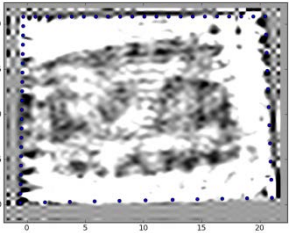
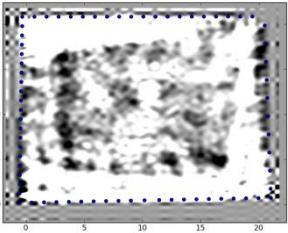
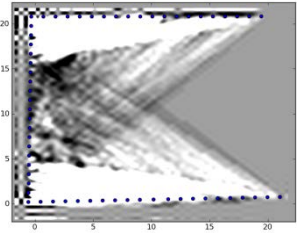
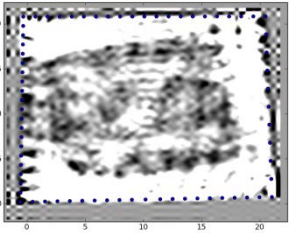
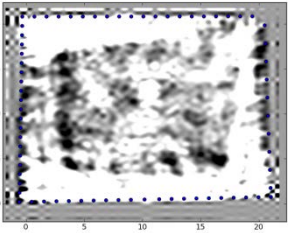
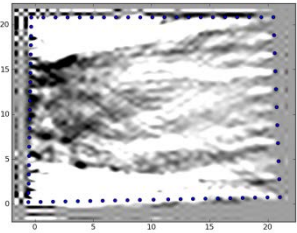
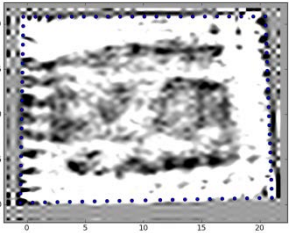
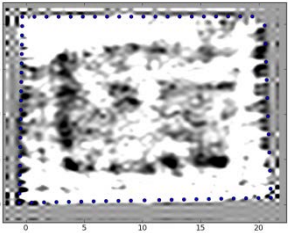
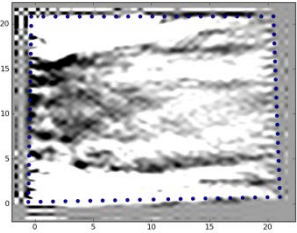
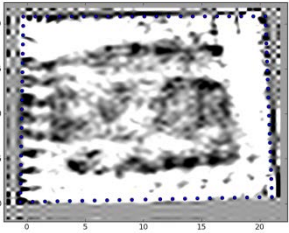
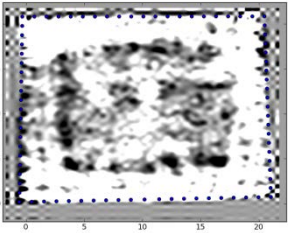
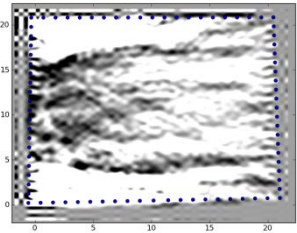
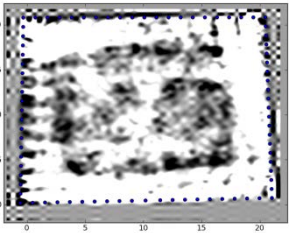
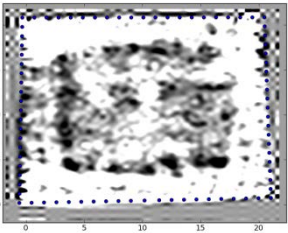
## Conclusions and Future Work

In this project we have investigated the theoretical models for RF tomography, constructed and fielded an RF tomography testbed, and reconstructed the floorplan of a structure using only RSS measurements. While there were numerous challenges using the data collected during the field test, we have successfully demonstrated that radio frequency (RF) tomography can be applied to imaging the floor plans of buildings. We have analyzed the problems with the data collected and determined the modifications to the testbed to avoid these problems in future collections. In spite of these problems we have demonstrated that RF tomography can be used to estimate the floorplan of a structure with significant structural details.

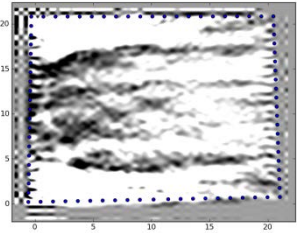
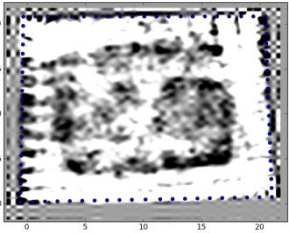
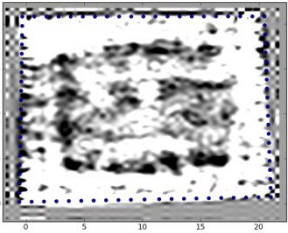
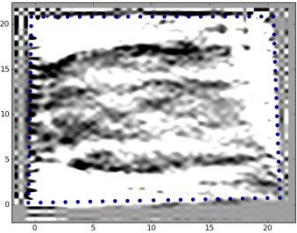
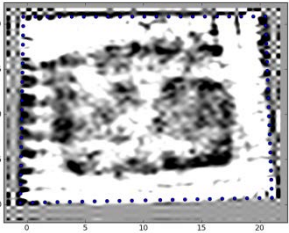
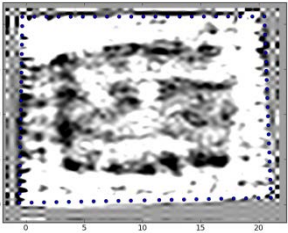
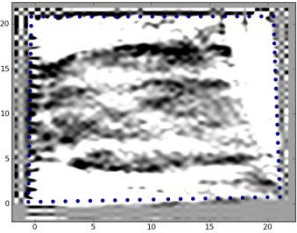
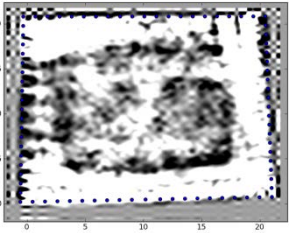
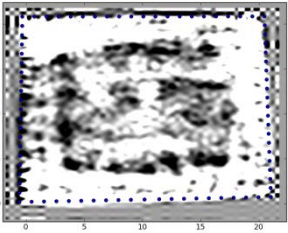
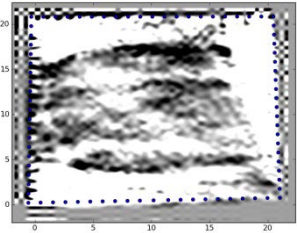
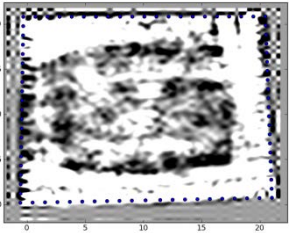
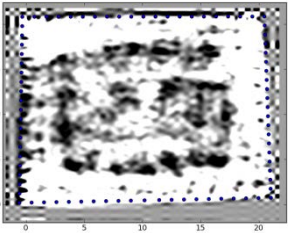
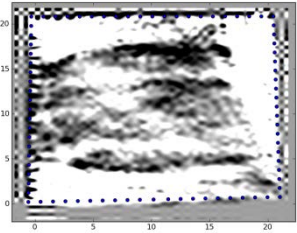
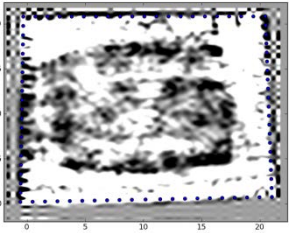
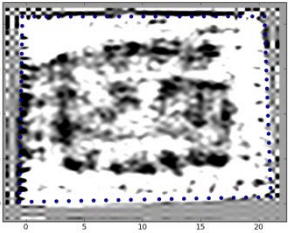
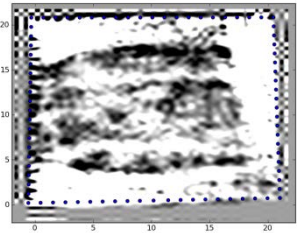
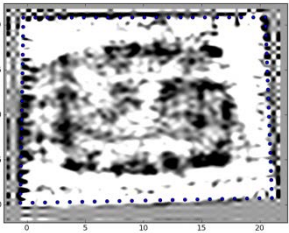
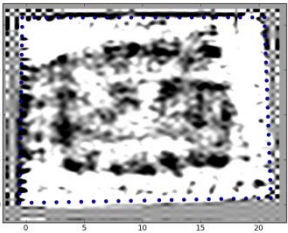
Despite the success of this project in demonstrating the viability of this concept, there is still more study needed to improve both the robustness and capabilities of this imaging modality. We have shown that two tomographic projection models provide reasonable results. Further study is necessary to determine which better models the physical reality. Additionally, the cause of the artifacts in the reconstructed floorplan image cannot be determined from the collected data. Further field tests will be needed to determine the root cause of these artifacts and correct for them. Experience from the field test measurements has also inspired further research. With more precise position information for the transmitting and receiving antennas, we hope to achieve imaging resolution of less than one wavelength. Further theoretical and technical investigation will be needed to evaluate this hypothesis.

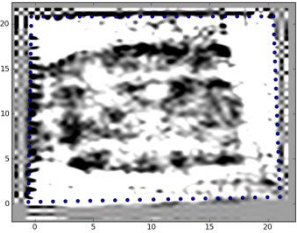
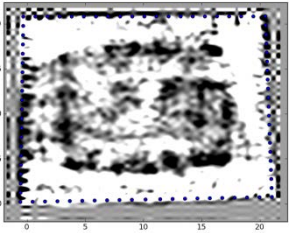
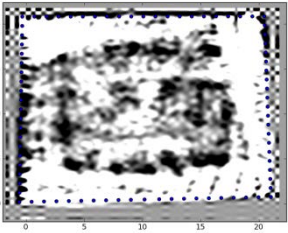
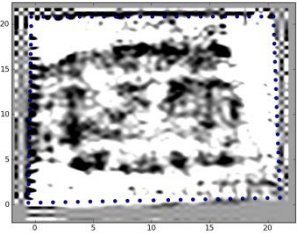
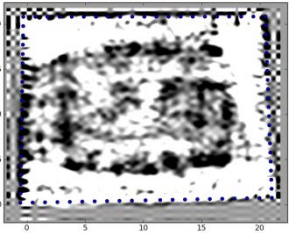
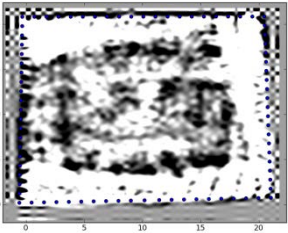
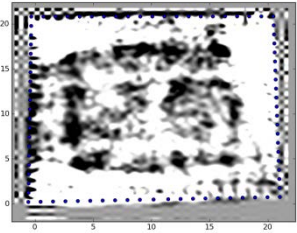
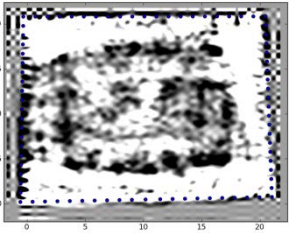
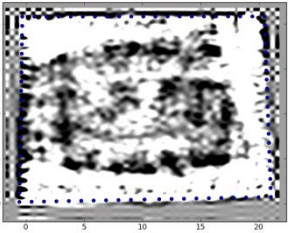
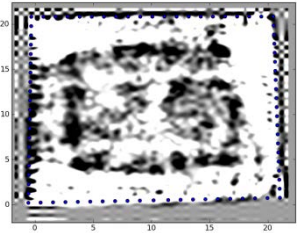
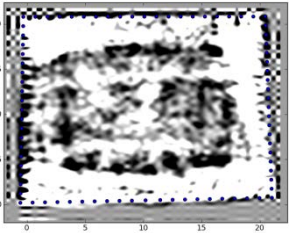
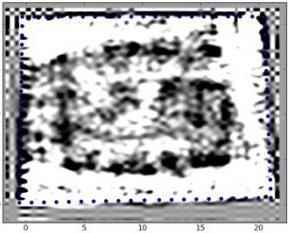
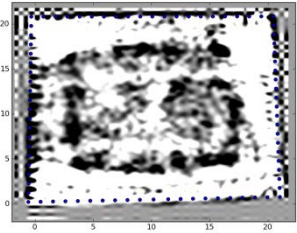
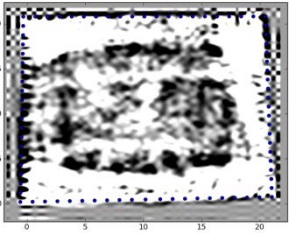
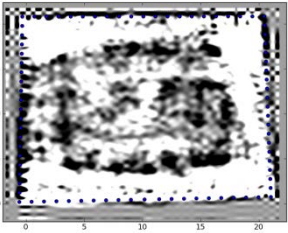
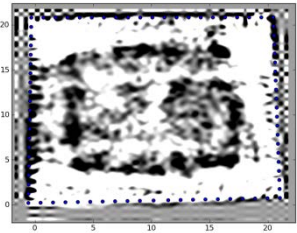
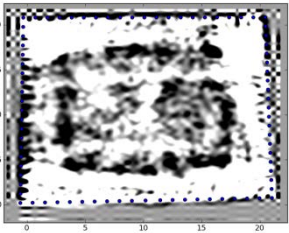
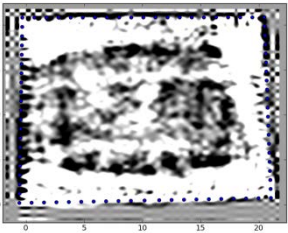
## Appendix A: Image Reconstruction Progression (Different Orderings)

	Steps 1-24	Steps (Most Independent) 1, 5, 9, 13, 17, 21, 2, 6...24	Steps (Random) 18, 19, 5, 2, 11, 23, 4, 6, 10, 13, 8, 9, 1, 16, 17, 3, 14, 21, 15, 12, 20
1			
2			
3			
4			
5			

6			
7			
8			
9			
10			
11			



12			
13			
14			
15			
16			
17			

18			
19			
20			
21			
22			
23			

24

